El Bakry Mahmoud, Ahmed Saad; Leinweber, Derek Bruce; Moran, Peter John; Sternbeck, André; Williams, Anthony Gordon
String effects and the distribution of the glue in static mesons at finite temperature Physical Review D, 2010; 82(9):094503

http://link.aps.org/doi/10.1103/PhysRevD.82.094503

String effects and the distribution of the glue in static mesons at finite temperature

A. S. Bakry,[1,*] D. B. Leinweber,[1] P. J. Moran,[1] A. Sternbeck,[2,1] and A. G. Williams[1]

[1]*Special Research Center for the Subatomic Structure of Matter, Department of Physics, University of Adelaide, South Australia 5005, Australia*

[2]*Institut für Theoretische Physik, Universität Regensburg, D-93040 Regensburg, Germany*

(Received 5 May 2010; published 8 November 2010)

The distribution of the gluon action density in mesonic systems is investigated at finite temperature. The simulations are performed in quenched QCD for two temperatures below the deconfinement phase. Unlike the gluonic profiles displayed at $T = 0$, the action-density isosurfaces display a prolate-spheroid-like shape. The curved width profile of the flux tube is found to be consistent with the prediction of the free bosonic string model at large distances.

DOI: 10.1103/PhysRevD.82.094503 PACS numbers: 12.38.Gc, 12.38.Lg, 12.38.Aw

I. INTRODUCTION

In the flux-tube model, the linearly rising potential between a pair of static color sources is believed to be due to the formation of a thin gluonic flux tube of a constant cross-section. At high temperatures, lattice simulations on pure SU(3) gauge fields [1] have indicated a decrease of the effective string tension for the quark–antiquark potential with the rise of the temperature. The QCD vacuum structure around the sources is then expected to exhibit gluonic profiles with widths variant to the zero temperature case. The detailed geometry of the gluonic field at finite temperature and whether it holds the constant cross-section property is an interesting topic that has not yet been explored in lattice quantum chromodynamics.

The low-energy dynamics of the flux tubes in the infrared region of a confining gauge theory can be described in terms of an effective bosonic string. The thin flux tube between two widely separated static color sources fluctuates like a massless string. The linearly rising part of the potential arises from the classical configuration which corresponds to the flat world sheet of the string. The quantum fluctuations of the string lead to a universal subleading correction to the potential well known as the Lüscher term [2]. Lattice simulations for several gauge theories [3–7] have supported the existence and the universality of the string's subleading effect. At high temperatures, the gluonic modes come into play and the effective string description of the temperature-dependent quark–antiquark potential has been worked out in Refs. [8,9]. A further comparison with SU(3) Monte Carlo lattice data for temperatures beginning from $T = 0.8T_c$ [1] has shown a good parametrizing behavior to the string picture formula for a minimal distance of $RT = 0.5$. On the other hand, there have been numerical indications that the inclusion of the higher-order string effects beyond the Gaussian approximation, e.g., the NLO string's self-interaction term in the Nambu-Goto effective string action, has reproduced the correct temperature-dependent string tensions up to a temperature scale of $T = 0.5T_c$ in the three-dimensional gauge Z_2 model [10].

The string model predictions of a logarithmic broadening [11] for the width of the string delocalization have also been observed in several lattice simulations corresponding to different gauge groups [4,6,12,13]. As the temperature increases, substantial deviations from the logarithmic behavior are expected, and the law of broadening turns eventually into a linear growth for large distances before the deconfinement is reached from below [14]. Apart from the peculiar features in the law of the broadening of the flux tube when the temperature is raised, the string picture predicts an effect which is rather interesting from the geometrical point of view. The width calculated at each corresponding transverse plane to the line joining the two quarks is found to differ from that at the central plane by an amount that increases with the rise of the temperature. In other words, the mesonic string picture is implying a curvature in the gluonic profile that becomes more pronounced as higher temperatures are approached. The string self-interaction with the quark line causes a noticeable difference in the delocalizations beyond the central transverse plane and these aspects remain to be ascertained in lattice quantum chromodynamics. Moreover, revealing the whole profile of the glue at finite temperature provides a particularly interesting source of knowledge regarding the true geometry of the flux tube, since, naturally, at finite temperature one need not hold to any particular assumption for the shape of the gluonic source-wave functions in the relevant gauge-invariant objects representing the quark states. Probing the transverse profile of the glue might even be of relevance to the modeling of ground-state sector of the theory where the exact geometry of the flux tube seems to be not yet settled [15].

In this paper, we investigate the distributions of the color field inside a static meson at two temperatures below the deconfinement phase, $T \simeq 0.9T_c$, and $T \simeq 0.8T_c$. Since the bosonic string predictions are expected to be more relevant

*abakry@physics.adelaide.edu.au

to pure Yang-Mills theories with static color sources (rather than QCD with dynamical sea quarks where string breaking occurs), the lattice simulations are performed on the SU(3) gauge group in the quenched approximation. The field strength inside the corresponding quark system will be revealed by correlating an improved action-density operator [16] to the mesonic state. The static mesonic state is accounted for by means of Polyakov-loop correlators. Gauge smoothing [17,18], in addition to a high statistics gauge-independent approach [19], will be employed to enhance the signal to the noise in the flux correlation function. This noise-reduction approach is variant to other approaches that utilize gauge fixing [20]. The obtained profile of the action density will then be compared to the prediction of the mesonic string models at several distances for the highest temperature near the deconfinement point $T \simeq 0.9T_c$.

The paper is organized as follows: In Sec. II, the details of the simulation will be described. We review the predictions of the bosonic string model for the $q\bar{q}$ potential and the width of the string fluctuations at finite temperature in Sec. III. In Sec. IV A, we measure the quark–antiquark potential and examine the string model parametrization for various levels of gauge smoothing. In Sec. IV B, the action density in mesons will be presented, and the corresponding widths at several transverse planes to the tube are then measured and set in comparison with the string model predictions. Section V provides the conclusion.

II. SIMULATION DETAILS

A. Color field measurements

In this investigation we have taken our measurements on 500 quenched QCD gauge-field configurations for each set of lattice parameters considered. The gauge configurations were generated using the standard Wilson gauge action on lattices with spatial volume of 36^3. We chose to perform our analysis with lattices as fine as $a = 0.1$ fm by adopting a coupling of value $\beta = 6.00$, with temporal extents of $N_t = 8$ and $N_t = 10$ slices, which correspond to temperatures $T \simeq 0.9T_c$ and $T \simeq 0.8T_c$, respectively. The gluonic gauge configurations were generated with a pseudo–heat bath algorithm [21,22] updating the corresponding three SU(2) subgroup elements [23]. Each update step consists of one heat bath and 4 microcanonical reflections. The measurements are taken after each 2000 of updating sweeps.

The static mesonic state is constructed by means of a pair of Polyakov loops corresponding to an infinitely heavy quark–antiquark pair,

$$\mathcal{P}_{2Q}(\vec{r}_1, \vec{r}_2) = P(\vec{r}_1)P^{\dagger}(\vec{r}_2),$$

where the Polyakov loop is given by

$$P(\vec{r}_i) = \frac{1}{3}\,\mathrm{Tr}\Big[\prod_{n_t=1}^{N_t} U_{\mu=4}(\vec{r}_i, n_t)\Big], \tag{1}$$

and the vectors $\vec{r}_i$ define the positions of the quarks. The measurements that characterize the color field are taken by a gauge-invariant action-density operator $S(\vec{\rho}, t)$ at spatial coordinate $\vec{\rho}$ of the three-dimensional torus corresponding to a Euclidean time t. The measurements are repeated for each time slice and then averaged,

$$S(\vec{\rho}) = \frac{1}{N_t}\sum_{n_t=1}^{N_t} S(\vec{\rho}, t). \tag{2}$$

The action-density operator is calculated via a highly improved $\mathcal{O}(a^4)$ three-loop improved lattice-field-strength tensor [16]. A dimensionless scalar field that characterizes the gluonic field can be defined as

$$\mathcal{C}(\vec{\rho}; \vec{r}_1, \vec{r}_2) = \frac{\langle \mathcal{P}_{2Q}(\vec{r}_1, \vec{r}_2)\rangle\langle S(\vec{\rho})\rangle - \langle \mathcal{P}_{2Q}(\vec{r}_1, \vec{r}_2) S(\vec{\rho})\rangle}{\langle \mathcal{P}_{2Q}(\vec{r}_1, \vec{r}_2)\rangle\langle S(\vec{\rho})\rangle}, \tag{3}$$

where $\langle \ldots\ldots \rangle$ denotes averaging over configurations and lattice symmetries, and the vector $\vec{\rho}$ refers to the spatial position of the flux probe with respect to some origin. Cluster decomposition of the operators leads to $C \rightarrow 0$ away from the quarks.

B. Noise reduction

We make use of translational invariance by computing the correlation on every node of the lattice, and averaging the results over the volume of the three-dimensional torus, in addition to averaging the action measurements taken at each time slice in Eq. (2). To further improve the signal to noise ratio in the gluonic correlation function, local action reduction by smearing the gauge links has been performed on the whole four-dimensional lattice. Since the main focus in this investigation is to resolve the nature of the flux distributions in the IR region of the theory, we have been able to show that with an appropriate level of gauge smoothing, effects on the large distance correlations can be kept minor. For each distance scale, a range of smoothing levels is seen to leave physical observables and topological structures intact. Similar techniques have been adopted in Ref. [24] in the determination of the large distance $Q\bar{Q}$ force in vacuum with different levels of hypercubic (HYP) smearing. In Sec. IV A, it has been shown that for a given distance scale, the measured quark–antiquark force at large distances can be left with negligible changes for a range of smoothing levels. Unlike [25] where the Cabbibo-Marinari cooling has been employed, we have chosen to smooth the gauge field by an overimproved stout-link smearing algorithm [18]. The use of this algorithm should ensure that the smoothing algorithm has a minimal effect on the topology of the gauge field [18]. In standard stout-link smearing [17], all the links are simultaneously updated. Each sweep

of update consists of a replacement of all the links by the smeared links

$$\tilde{U}_\mu(x) = \exp(iQ_\mu(x))U_\mu(x), \tag{4}$$

with

$$Q_\mu(x) = \frac{i}{2}(\Omega_\mu^\dagger(x) - \Omega_\mu(x)) - \frac{i}{6}\,\mathrm{tr}(\Omega_\mu^\dagger(x) - \Omega_\mu(x)),$$

and

$$\Omega_\mu(x) = \Big(\sum_{\nu\neq\mu}\rho_{\mu\nu}\Sigma_{\mu\nu}^\dagger(x)\Big)U_\mu^\dagger(x),$$

where $\Sigma_{\mu\nu}(x)$ denotes the sum of the two staples touching $U_\mu(x)$ which reside in the μ-ν plane. The scheme of overimprovement requires $\Sigma_{\mu\nu}(x)$ to be replaced by a combination of plaquette and rectangular staples. This ratio is tuned by the parameter ϵ [18]. In the following we use a value of $\epsilon = -0.25$, with $\rho_\mu = \rho = 0.06$. We note that for a value of $\rho = 0.06$ the overimproved stout-link algorithm is roughly equivalent in terms of UV filtering to the standard stout-link smearing algorithm with the same $\rho = 0.06$.

III. THE BOSONIC STRING MODEL

A. Temperature-dependent quark–antiquark potential

The correlation function of two Polyakov loops on the lattice determines the interaction potential between the color sources,

$$\langle P(0)P^\dagger(R)\rangle = \int d[U]P(0)P^\dagger(R)\exp(-S_w) = \exp(-V(R,T)/T). \tag{5}$$

S_w is the plaquette action and T is the physical temperature. The self-interactions of the glue exchanged between two color sources in QCD can result in the squeezing of the glue into a thin one-dimensional stringlike object. The immediate consequence of this string picture is that a functional form can be ascribed to the Polyakov-loop correlators, namely, the partition function of the string. The correlators are expressed as functional integrals over all the world sheet configurations swept by the string,

$$\langle P(0)P^\dagger(R)\rangle = \int_{\mathcal{C}}[DX]\exp(-S(X)). \tag{6}$$

The vector $X^\mu(\zeta_1,\zeta_2)$ maps the region $\mathcal{C}\subset R^2$ into R^4, with Dirichlet boundary condition $X(\zeta_1,\zeta_2=0) = X(\zeta_1,\zeta_2=R) = 0$, and periodic boundary condition along time direction $X(\zeta_1=0,\zeta_2=0) = X(\zeta_1=L,\zeta_2=R)$, and S is the string action and can be chosen to be proportional to the surface area, i.e., the Nambu-Goto action,

$$S[X] = \sigma\int d\zeta_1\int d\zeta_2\sqrt{g}, \tag{7}$$

where $g_{\alpha\beta}$ is the two-dimensional induced metric on the world sheet embedded in the background $\mathbb{R}^4$,

$$g_{\alpha\beta} = \frac{\partial X}{\partial\zeta_\alpha}\cdot\frac{\partial X}{\partial\zeta_\beta}, \qquad (\alpha,\beta=1,2), \qquad g = \det(g_{\alpha\beta}).$$

Gauge fixing is required for the path integral (9) to be well defined with respect to Weyl and reparametrization invariance. The physical gauge, $X^1 = \zeta_1$, $X^4 = \zeta_2$ would restrict the string fluctuations to transverse directions to $\mathcal{C}$. In the quantum level, Weyl invariance is broken in 4 dimensions; however, the anomaly is known to vanish at large distances [26]. The action after gauge fixing reads

$$S[X] = \sigma\int_0^L d\zeta_1\int_0^R d\zeta_2(1+(\partial_{\zeta_1}X_\perp)^2+(\partial_{\zeta_2}X_\perp)^2)^{1/2}. \tag{8}$$

Expanding the square root in powers of σRL,

$$S[X] = \sigma RL + \frac{\sigma}{2}\int_0^L d\zeta_1\int_0^R d\zeta_2(\nabla X_\perp)^2 + \ldots, \tag{9}$$

the action decomposes into the classical configuration and fluctuation part, and the string higher-order self-interactions. A leading-order approximation can be made by neglecting the self-interaction terms; the path integral Eq. (9) is then

$$\langle P(0)P^\dagger(R)\rangle = e^{-\sigma RL}\Big[\det\Big(-\frac{1}{2}\nabla^2\Big)\Big]^{-1}. \tag{10}$$

The determinant of the Laplacian on the cylinder has been regulated using a lattice regulator in [8]. The potential is obtained in closed form for a length scale comparable to the thermodynamic scale in [9]. The effective potential is

$$V(R,T) = \Big(\sigma - \frac{\pi}{3}T^2 + \frac{2}{3}T^2\tan^{-1}(2RT)^{-1}\Big)R - \Big(\frac{\pi}{12} - \frac{1}{6}\tan^{-1}(2RT)\Big)\frac{1}{R} - \frac{T}{2}\log(1+(2RT)^2) + \mu. \tag{11}$$

The limit of large string length [8] entails taking the temperature-dependent string tension to be

$$\sigma(T) = \sigma - \frac{\pi}{3}T^2. \tag{12}$$

The free-string model predicts a temperature-dependent quark–antiquark potential that is featured by the existence of a logarithmic term in addition to a leading-order decrease in the string tension by an amount $\frac{\pi}{3}T^2$.

B. Width of the flux-tube fluctuations at finite temperature

The vibration modes of the stringlike object render an effective width for the flux tube. A well known prediction made by Lüscher, Münster, and Weisz [11], based on the

effective bosonic string model, has shown that the mean-square width of the vibrating flux tube at the center plane grows logarithmically as a function of the interquark separation, R,

$$w^2 \sim \frac{1}{\pi\sigma}\log\left(\frac{R}{\lambda}\right), \tag{13}$$

where λ is an ultraviolet scale. With the increase of the temperature, higher-order gluonic degrees of freedom are present and the effective width of the corresponding string is expected to manifest an intricate behavior involving both the distance and the temperature. The mean-square width of the string is defined as

$$w^2(\xi;\tau) \equiv \langle X^2(\xi;\tau)\rangle = \frac{\int_C [DX] X^2 \exp(-S[X])}{\int_C [DX]\exp(-S[X])}. \tag{14}$$

$\xi = (\xi_1, i\xi_2)$ is a complex parametrization of the world sheet, such that $\xi_1 \in [-R/2, R/2]$, $\xi_2 \in [-L/2, L/2]$, with $\tau = \frac{L}{R}$ is the modular parameter of the cylinder, and L is the temporal extent governing the inverse temperature. Casselle *et al.* [6] and Gliozi [27] have worked out the delocalization of the string for all the planes transverse to the line joining the quark pair by the corresponding Green function. This technique proceeds by removing the divergence in the quadratic operator in Eq. (14) by the use of the Schwinger [28] point-split regularization, then taking the limiting action for the Nambu-Goto model as that of the corresponding Gaussian model. The quadratic operator is then the correlator of the free bosonic string theory in two dimensions,

$$\langle X^2(\xi;\tau)\rangle \equiv \langle X(\xi)\cdot X(\xi+\epsilon)\rangle = G(\xi, \xi+\epsilon). \tag{15}$$

This Green function is the solution of the Laplace equation on the cylinder with a Dirichlet boundary condition,

$$G(\xi, \xi_0) = \frac{-1}{2\pi}\log|f(\xi, \xi_0)|. \tag{16}$$

The conformal map reads [14]

$$f(\xi, \xi_0) = \frac{\theta_1[\pi(\xi-\xi_0)/R;\tau]}{\theta_2[\pi(\xi-\xi_0)/R;\tau]}, \tag{17}$$

where the Jacobi θ functions are

$$\begin{aligned}\theta_1(\xi;\tau) &= 2\sum_{n=0}^{\infty}(-1)^n q^{n(n+1)+(1/4)}\sin((2n+1)\xi),\\ \theta_2(\xi;\tau) &= 2\sum_{n=0}^{\infty} q^{n(n+1)+(1/4)}\cos((2n+1)\xi),\end{aligned} \tag{18}$$

with the nome $q = e^{(-\pi/2)\tau}$. The expectation value of the mean-square width would then read

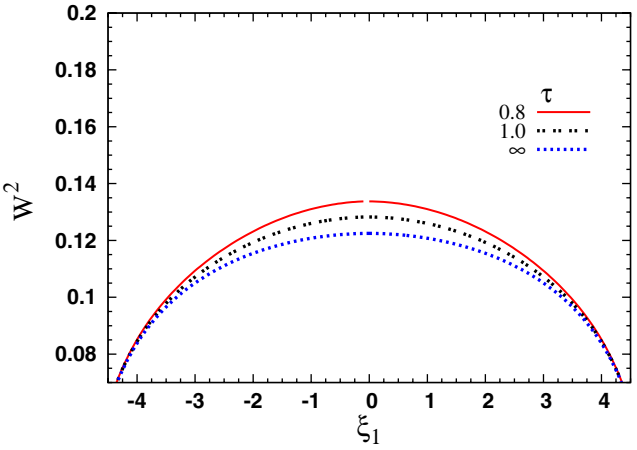

FIG. 1 (color online). The mean-square width, Eq. (19), of the flux tube evaluated at all planes ξ_1 perpendicular to the quark–antiquark line. The separation distance between the pair is $Ra^{-1} = 10$.

$$w^2(\xi_1,\tau) = \frac{1}{2\pi\sigma}\log\left(\frac{R}{R_0}\right) + \frac{1}{2\pi\sigma}\log\left|\frac{\theta_2(\pi\xi_1/R;\tau)}{\theta_1'(0;\tau)}\right|. \tag{19}$$

This expression converges for modular parameters close to 1, and contains in addition to the logarithmic divergence term a correction term that encodes the dependence of the width at different transverse planes on the modular parameter of the cylinder. At finite temperature, this term is contributing to the width at all the planes. Figure 1 is a plot of the mean-square width calculated at ξ_1 values via Eq. (19). The plot shows the profile for several modular parameters and fixed separation between the two Polyakov loops.

The string model predicts an increase in the width with the increase of the temperature. The increase in the width is maximum at the central plane which is seen as an increase in the curvature in the profile of the string fluctuations. At zero temperature $L \to \infty$, Eq. (19) converges well, and the second term in Eq. (19) still contributes to the whole shape of the fluctuations at all planes except the middle; the contribution of this term at zero temperature is

$$\frac{1}{2\pi}\log\left|\cos\left(\frac{\pi\xi_1}{R}\right)\right|, \tag{20}$$

which is seen from the plot of Fig. 1 to be subtle in the middle region and have more pronounced effects on the width near the quark positions.

IV. RESULTS

A. Quark–antiquark potential

The technique adopted to enhance the signal to the noise in the correlation function which characterizes the gluon

flux, Eq. (3), involves smoothing the gauge links by the overimproved stout-link smearing algorithm described above. The whole 4-dim torus has been smeared for the consecutive levels of smearing corresponding to 20, 40, 60, and 80 sweeps, forming four data sets for each temperature. The choice of the appropriate data set for the numerical evaluation of the expectation values in Eq. (3) at each distance scale should be based on a compromise to simultaneously achieve two tasks, that the smearing level has a minimal effect on the physical observables, and a significant error reduction is gained. The larger the separation distance between the quark pair, the higher the smearing level required to gain good signal to noise in the correlations in Eq. (3). However, smearing has an effect on the observables similar to the increase of the lattice space-time cutoff, and a large enough number of smearing sweeps will result in a subsequent loss of the physics on the short distance scale. The physical observable of direct relevance to the properties of the gluonic flux tube is the quark–antiquark potential. For each level of smearing, we numerically evaluate the quark–antiquark potential and the corresponding force. At fixed temperature T, the Monte Carlo evaluation of the quark–antiquark potential at each R is calculated through the Polyakov-loop correlators according to

$$V(R,T) = \frac{-1}{T}\log(\langle P(0)P^{\dagger}(R)\rangle). \tag{21}$$

The jackknife error analysis for the data shows a significant decrease in the uncertainties associated with Polyakov-loop correlators on a short distance scale when measurements are taken after 20 sweeps of smearing. For large distances, a subsequent increase of 20 sweeps would provide error reduction by factors of $1.3 \leq x \leq 1.5$ for the corresponding distances 0.6 fm $\leq R \leq$ 1 fm. Table I summarizes the factors of error reduction for the Polyakov-loop correlator after each incremental increase of 20 sweeps of smearing [29].

To test the validity of the gauge-smoothing approach, or, equivalently, to determine the levels of smoothing for which the physics is left intact, one is tempted to set a reference scale which signifies how the smeared data would behave with respect to it. Here, we set this scale to be the string model parametrization Eq. (11). This approach of referencing the data to the string model is justified by the fits previously reported in Ref. [1], which has returned good χ^2 and shown stability to the fit range at large distances.

TABLE I. The error reduction factor in the Polyakov-loop correlator Eq. (5) by the increase of the number of 20 smearing sweeps for each smeared data set.

R/Number of sweeps	20–40	40–60	60–80
6	1.3	1.1	1.1
8	1.4	1.2	1.2
10	1.5	1.3	1.2

The numerical data obtained for the quark–antiquark potential Eq. (21) on every smoothed gauge configuration are fitted to the string picture $q\bar{q}$ potential Eq. (11). The effects of smearing are expected to be more pronounced at short distances. For this reason the minimal fit distances are taken as large as possible, $R > 0.7$ fm for $T = 0.8T_c$, and $R > 0.9$ fm for $T = 0.9T_c$. The string tension has been taken as a fitting parameter. The fits are returning good χ^2 for all the smoothed data sets considered.

The $q\bar{q}$ potential and the corresponding fits are shown in Fig. 2. The fits to the data show almost equal slopes for all smoothing levels. This is also manifest in Table II, where the string tensions are measured in accord to Eqs. (11) and (12). Within the standard deviations of the measurement, the returned string tensions for all levels of smearing are equal. At temperature $T = 0.9T_c$, our measurements for

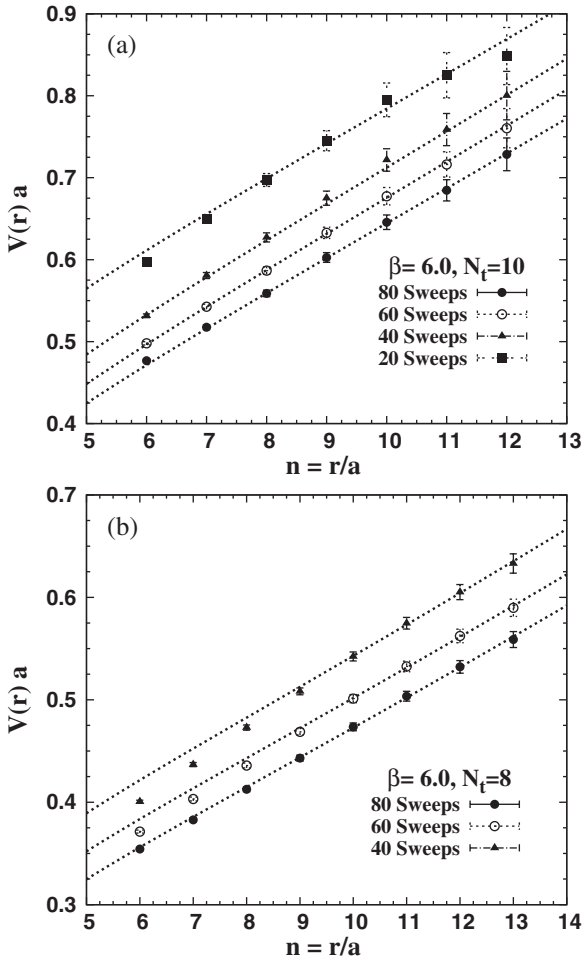

FIG. 2. The quark–antiquark potential measured at each depicted smearing level. The lines correspond to fits of the potential obtained from the string picture of Eq. (11) for each data set as described in the text. The upper plot is at $T = 0.8T_c$ while the lower plot is at $T = 0.9T_c$.

TABLE II. The string tension measured on all data sets corresponding to various levels of link smearing. The measurements are obtained from the fits to Eqs. (11) and (12).

Number of sweeps	σa^2	Fit range $n = R/a$
$T = 0.8T_c$		
20	0.047(3)	8–12
40	0.050(2)	8–12
60	0.0493(9)	8–12
80	0.0478(6)	8–12
$T = 0.9T_c$		
40	0.0385(8)	10–13
60	0.0377(9)	10–13
80	0.0373(8)	10–13

the string tension agree for all the data sets. Moreover, this value is in agreement with that reported in Ref. [1].

The factors of error reduction at higher temperature at $R = 1$ fm after 40 sweeps of smearing compare to the corresponding one at $T = 0.8$ after 80 sweeps. The noise tends to decrease with the increase of the temperature. This analysis shows that for the $q\bar{q}$ separation distance $R \geq 1$ fm as depicted in Table II, all the smoothed configurations are appropriate for revealing the gluonic field. On the other hand, it is clear that the data points for $R \leq 0.8$ fm shift up with the increase of the number of smearing sweeps. The removal of short distance physics is manifest here [31]. The difference in the regularization brought about by the increasing of the space-time cutoff introduced by smearing shifts the $q\bar{q}$ potential by a renormalization constant in Eq. (21). To illustrate the effect of smearing on the $q\bar{q}$ potential, the potential Eq. (21) has not been normalized. The $q\bar{q}$ force, however, can be calculated to

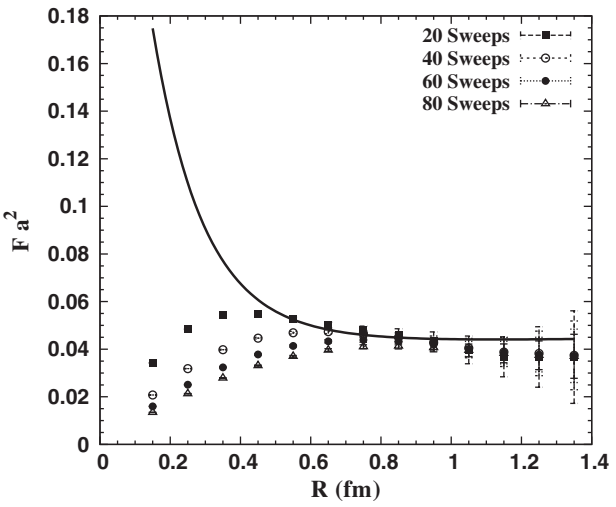

FIG. 3. The $q\bar{q}$ force measured for all the smearing levels up to a distance of 1.4 fm. The temperature is $T = 0.8T_c$, and $\beta = 6$. The line denotes the force as predicted by the string model at finite temperature, Eq. (11).

TABLE III. The characteristic radii R_s and R_F at each smearing level.

Number of sweeps	R_F (fm)	R_s (fm)	$2R_s$ (fm)
20	0.55	0.27	0.54
40	0.65	0.38	0.76
60	0.75	0.47	0.94
80	0.95	0.54	1.04

eliminate these constant shifts. With the definition of the derivative on the lattice taken as in Refs. [3,32], the force is computed as

$$F\left(r - \frac{a}{2}\right) = \frac{V(r) - V(r-a)}{a}. \tag{22}$$

Figure 3 shows the force calculated for all smearing levels for distances up to 1.4 fm. The force from the string picture, Eq. (11), with a fit parameter measured at 60 sweeps in Table II is illustrated. Inspection of Figs. 2 and 3 enables one to estimate a distance scale beyond which effects of smearing are negligible. For example, the results for 20 sweeps and 40 sweeps of smearing agree for $R \geq 0.65$ fm in Fig. 3. Similar comparisons of 40 and 60 sweeps or 60 and 80 sweeps provide the results, R_F, depicted in Table III. This also can be read in conjunction with the radius of Brownian motion or the so-called smearing radius. For the standard APE smearing [33] this quantity can be calculated analytically [34] (see also Appendix A), and may then be calibrated [35] to the improved stout-link smearing algorithm used here. This gives a smearing radius

$$R_s = a\sqrt{c\rho n_s}, \tag{23}$$

where n_s denotes the number of smearing sweeps and $c = 6.15(3)$ is the calibration constant calculated in Appendix B. In Fig. 4 the smearing radius is plotted versus the number of smearing sweeps. R_s describes the characteristic scale of smearing, within which the gluon action density has been suppressed. Values for R_s are compared to R_F in Table III, where the radius threshold for agreement of the $q\bar{q}$ force, R_F, lies close to the smearing diameter $2R_s$,

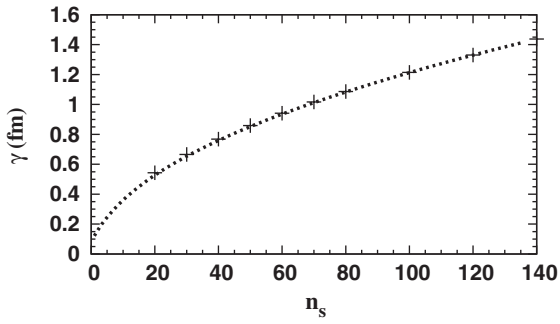

FIG. 4. The diameter of smearing $2R_s$ versus the number of sweeps n_s [Eq. (23)] for the improved stout-link algorithm with $\rho = 0.06$ [Eq. (23)].

which is the minimal distance between two diffuse links in Polyakov-loop correlators. Therefore, a conservative range of trust for distance scales where the essential features of the confinement remain unchanged for a given level of gauge smoothing can be provided by

$$\gamma = 2R_s. \tag{24}$$

A combination of a large number of Monte Carlo updates followed by link averaging has been performed in Ref. [1] to evaluate the $q\bar{q}$ potential for a range of temperatures above and below the confinement phase. This involves a large number of updating sweeps and measurements which makes it rather expensive in terms of the CPU time. This is particularly true for the evaluation of the gluonic flux distribution, since this concerns the Monte Carlo evaluation of not only the Polyakov-loop correlator, but also the three-point correlation function in the numerator of Eq. (3). Gauge smoothing is chosen as a cheap and effective method in this case to reveal the general topological features of the flux distribution which can be confronted with the predictions of the string model. We have been able to show in this section the ranges of the validity of this approach, through the measurements of the physical observables that have been previously reported in [1], i.e., the $q\bar{q}$ potentials and the string tension.

B. Action density

1. Tube profile (qualitative picture)

The lattice operator which characterizes the gluonic field is usually taken as the correlation between the vacuum action density $S(\vec{\rho}, t)$, and a gauge-invariant operator representing the quark states. At finite temperature this must be a pair of Polyakov lines. The action-density operator is calculated through an $\mathcal{O}(a^4)$ improved lattice version of the continuum field-strength tensor. Discretization errors are reduced by combining several clover terms complemented by tadpole improvement [16]. We take our measurements with a three-loop field-strength tensor given by

$$F^{\mathrm{Imp}}_{\mu\nu} = \sum_{i=1}^{3} w_i C^{(i,i)}_{\mu\nu}, \tag{25}$$

where $C^{(i,i)}$ is a combination of Wilson-loop terms corresponding to loops with lattice extent i used to construct the clover term and w_i are weights [16]. The reconstructed action density,

$$S(\vec{\rho}) = \beta \sum_{\mu>\nu} \frac{1}{2} \mathrm{Tr}(F^{\mathrm{Imp}}_{\mu\nu})^2, \tag{26}$$

is accordingly measured on 20 sweeps of stout-link smearing. This has the effect of the removal of the divergence in the action density in the neighborhood of the quark positions. It is, however, very beneficial in obtaining a good signal to noise to display the flux strength.

The correlation function Eq. (3) provides $\mathcal{C}(\vec{\rho}) > 0$, and $\mathcal{C} \simeq 0$ away from the quark position. The scaled flux distribution $\bar{\mathcal{C}}(\vec{\rho}) = 1 - \mathcal{C}(\vec{\rho})$ in the plane of the $q\bar{q}$ pair is plotted in Figs. 5 and 6, for several $q\bar{q}$ separation distances $R = |\vec{r}_1 - \vec{r}_2|$, at temperature $T = 0.8T_c$. The

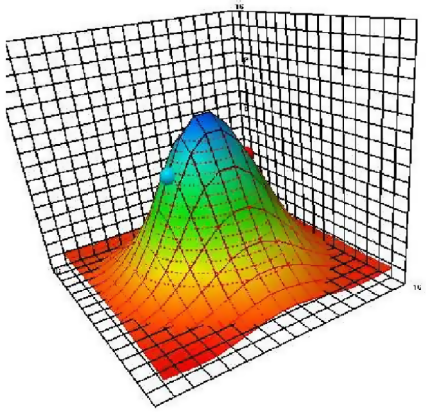

(a) $R = 5\ a$

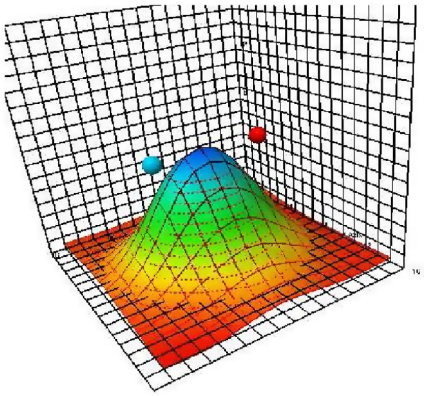

(b) $R = 6\ a$

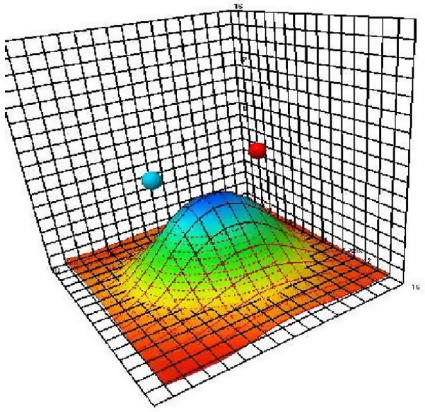

(c) $R = 7\ a$

FIG. 5 (color online). The flux-distribution $\bar{\mathcal{C}}(\vec{\rho}, \vec{r}_1, \vec{r}_2)$ as given by the characterization Eq. (3) in the plane of the quark–antiquark pair $\vec{\rho}(x, y, z = z_0)$, for separation distances R (a) 0.5 fm, (b) 0.6 fm, and (c) 0.7 fm at $T = 0.8T_C$. The spheres refer to the position of the quark and antiquark.

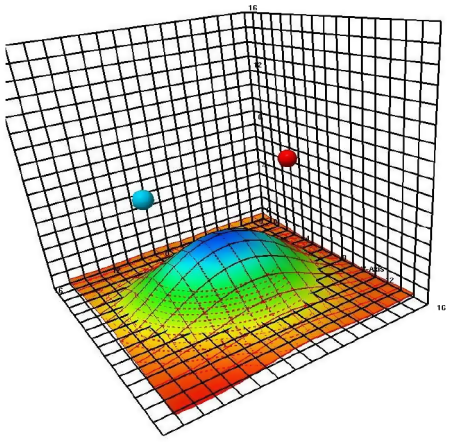

$R = 8\ a$

FIG. 6 (color online). Similar to Fig. 5 for source separation distances $R = 0.8$ fm.

Polyakov-loop correlator is measured on 40 sweeps of link smoothing. The distribution shows a peak in the middle point between the $q\bar{q}$ pair at small separation distance $R = 0.5$ fm. As the two quarks are pulled apart, the distribution $\mathcal{C}(\vec{\rho})$ decreases rapidly, the peak behavior diminishes, and the distribution is almost constant at $R = 0.8$ fm. The qualitative description of these density plots suggests a two-dimensional Gaussian-like behavior; however, as we will see in the next section, careful measurements of the widths at each perpendicular plane to the $q\bar{q}$ line yield different widths for large distances.

The behavior of the flux distribution around the outer edges of the density profile does depend on finite volume [36]. As a by-product of performing the simulations on large lattice sizes to gain high statistics in a gauge-independent manner, the two lattices employed in these investigations are of a typical spatial size of 3.6^3 fm^3 which does minimize the volume effect.

The curvature in the flux lines is manifesting itself as is evident from the flux-contour plots in Fig. 7. The contour plots reveal the form of the flux tube just before the deconfinement phase $T = 0.9T_c$, for $q\bar{q}$ sources separated by $R = 0.9$ fm and $R = 1$ fm, respectively. A similar plot of the action-density isosurface at $R = 0.9$ fm in Fig. 8 displays a three-dimensional version of Fig. 7 (prolate-spheroid-like shape) for the flux tube. This geometrical form of the density plot manifests itself at temperature $T = 0.8T_c$, which is known to be near the end of the plateau of the QCD-phase diagram [37].

It is worth noting, nevertheless, that at zero temperature the correlation of the action density with the Wilson loop taken as a mesonic operator does not reveal this curvature of the flux lines in the inner region between the $q\bar{q}$ pairs at large separation distance [4]. Thus we have illustrated how

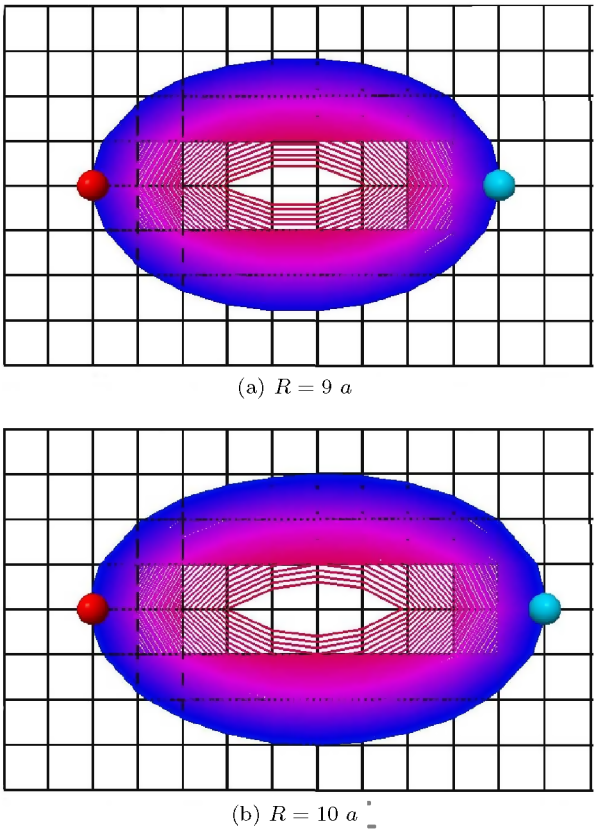

(a) $R = 9\ a$

(b) $R = 10\ a$

FIG. 7 (color online). The flux-contour-line distribution in the plane of the quark–antiquark pair z_0, for separation distances of (a) 0.9 fm, (b) 1.0 fm. The spheres denote the position of the $q\bar{q}$ pair, $T = 0.9T_C$.

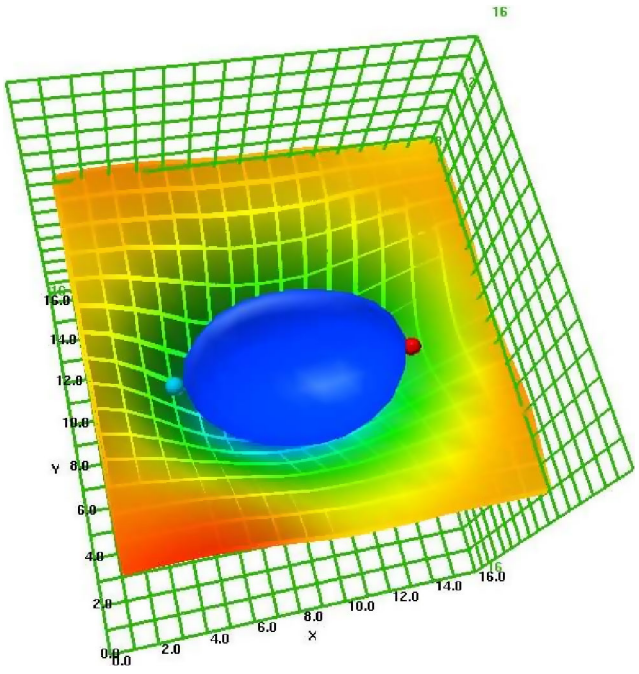

FIG. 8 (color online). The flux isosurface passing through the quarks, plotted together with a surface plot for the density distribution in the $q\bar{q}$ plane (inverted). The measurements are taken on 80 sweeps of smearing for separation distance $R = 9a$, and $T = 0.8T_c$. The lattice spatial extent is 36^3, $\beta = 6$.

thermal effects show up in the action-density correlations for the first time to the best of our knowledge [38].

2. Tube profile (quantitative aspects)

Usually studies carried out on the flux-tube laws of growth focus their measurements on the central plane transverse to the $q\bar{q}$ line. At $T = 0$, it seems also that there is a wide belief that the tube has almost a constant cross-section with a uniform energy-density profile for large $q\bar{q}$ separations. Nevertheless, at high temperature where the string tension is reported to decrease by a value around 10% at $T = 0.8T_c$ [1], our calculations of the flux chromostrength inside the meson (Figs. 5, 6, and 8) display a nonuniform action-density pattern around the whole $q\bar{q}$ line.

It was conceived a long time ago [40–42] that the QCD vacuum behaves like a dual superconductor, and the color field generated by a pair of quark sources is squeezed into a thin stringlike object dual to the Abrikosov vortex by the dual Meissner effect. It has been conjectured that this squeezed flux tube [2] can vibrate as a free string. At high temperature, one would expect higher modes relevant to the collective degrees of freedom of the stringlike object to give rise to new, interesting measurable effects, which seem not only to be related to the law of the growth of the tube's width [14], but also to the width's profile itself. The string model's solution, Eq. (19), informs us about how the tube would behave behind its symmetry point in the middle, and together with the observed chromofield profile (Figs. 5–8), one is tempted to investigate this string effect and establish a quantitative comparison between the model and the glue profile in QCD. This is the aim of this section.

Different possible components of the field-strength tensor in Eq. (25) can separately measure the chromoelectric and -magnetic components of the flux. The action density, however, is related to the chromofields via $\frac{1}{2}(E^2 - B^2)$ and is the quantity of direct relevance to the comparison with the string fluctuations [Eq. (14)]. The width of the flux tube may be then estimated through fitting the density distribution $\mathcal{C}(\vec{\rho})$ [Eq. (3)] in each selected transverse plane $\vec{\rho}(x_i, y, z_0)$ to a Gaussian [6,11].

The width of the tube is defined as

$$w^2(x_i) = \frac{\int d^2\eta \eta^2 e^{-(\eta^2/w^2)}}{\int d^2\eta e^{-(\eta^2/w^2)}}. \quad (27)$$

η is the set of vectors perpendicular to the $q\bar{q}$ line in the x_i plane. The flux calculations with Polyakov lines as a mesonic operator are well known to be distorted by statistical noise. To take reliable measurements to reveal the tube's fine structure, we choose to perform our analysis on the tube's width at the highest temperature $T = 0.9T_c$ where the scalar field $\mathcal{C}(\vec{\rho})$ has smaller jackknife error bars, even at very large distances. To further increase the signal to noise ratio, the number of measurements has been increased by a factor of 4. This has been done by updating each raw gauge configuration 3 times each separated by 70 sweeps of Monte Carlo updates as described in Sec. II. To avoid artificial reduction of the error bars, each set of four configurations (original configuration together with three new ones) has been included in the same jackknife subensemble, such that the variances are calculated with respect to decorrelated bins (see also Ref. [1]). The density distributions have been symmetrized around all the symmetry planes of the tube; the resultant average density $\mathcal{C}(\vec{\rho})$ is fit to a Gaussian of the form $A(x_i)e^{-(y-y_0)^2/w^2}$, with y_0 on the $q\bar{q}$ line (see. e.g., Fig. 9). The Gaussian fits to the data are for several transverse planes between two sources separated by a distance of $R = 12a$.

Table IV summarizes the measurements on both the widths $w^2(x_i)$ and the amplitudes $A(x_i)$ of the flux tube, in accord to these Gaussian fits at each transverse plane x_i to the $q\bar{q}$ line. The coordinates x_i are lattice coordinates (lattice units) and are measured from the quark position $x = 0$. The uncertainties in width measurements at each transverse plane are the standard asymptotic errors in the Gaussian fits and are correlated. The flux-density measurements at each source separation are taken on all smeared sets of configurations. We will be mainly discussing results for the set of configurations corresponding to 40 sweeps of smearing. According to Sec. IV A, this level of gauge smoothing leaves the $q\bar{q}$ potential and force with insignificant effects for $R > 0.6$ fm. We also discuss the effects of smearing on the gluonic profile. For a fixed source separation, the measured values in Tables IV and V (taken on 40 smearing sweeps) are indicating, generally speaking, changes in the tube width along the $q\bar{q}$ line. The maximum width is measured at the tube's symmetry point in the middle. At relatively small separations $R < 0.9$ fm, the change in tube width along the planes is subtle. The variation in the tube's width, however, is more pronounced at large source separation distances (see, e.g., Table V) in

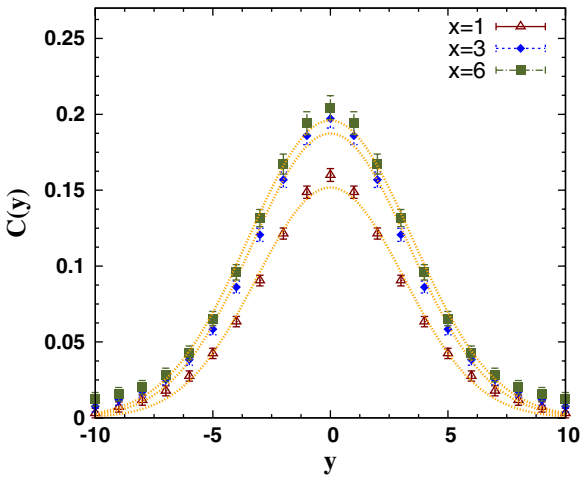

FIG. 9 (color online). The density distribution $\mathcal{C}(\vec{\rho})$ for separation distance of $R = 12a$, $T = 0.9T_c$, plotted for the transverse planes $x = 1$, $x = 3$, and $x = 6$. The lines correspond to the Gaussian fits to the density in each plane $\vec{\rho}(x_i, y, z_0)$.

TABLE IV. The width and the amplitude of the flux tube at each of the consecutive transverse planes x_i from the quark to the middle of the $q\bar{q}$ line. The measurements for sources' separation distances $R = 6a$ to $R = 9a$, for the temperature $T = 0.9T_c$.

Plane	$x = 1$		$x = 2$		$x = 3$		$x = 4$	
$n = R/a$	A	w^2a^{-2}	A	w^2a^{-2}	A	w^2a^{-2}	A	w^2a^{-2}
6	0.160(3)	14.6(5)	0.191(3)	14.4(5)	0.202(3)	14.4(5)		
7	0.165(3)	15.8(6)	0.199(3)	15.6(4)	0.218(4)	15.7(5)		
8	0.165(3)	16.9(6)	0.199(3)	17.0(5)	0.221(4)	17.1(5)	0.229(4)	17.2(5)
9	0.162(3)	17.9(6)	0.195(3)	18.2(6)	0.217(4)	18.6(6)	0.228(4)	18.8(6)

TABLE V. Similar to Table. IV, the widths of the flux tube are measured at each of the consecutive transverse planes x_i from the quark to the middle of the $q\bar{q}$ line. The measurements for sources' separation distances $R = 10a$ to $R = 13a$.

Plane	$x = 1$	$x = 2$	$x = 3$	$x = 4$	$x = 5$	$x = 6$
$n = R/a$	w^2a^{-2}	w^2a^{-2}	w^2a^{-2}	w^2a^{-2}	w^2a^{-2}	w^2a^{-2}
10	18.8(7)	19.4(6)	20.0(6)	20.4(6)	20.6(6)	
11	19.4(7)	20.3(7)	21.3(7)	22.0(7)	22.3(8)	
12	19.7(7)	21.0(7)	22.4(7)	23.4(8)	23.9(8)	24.1(9)
13	19.5(6)	21.0(7)	22.9(7)	24.4(8)	25.4(9)	25.8(9)

general qualitative agreement with the predictions of the string picture Fig. 1. The growth in width with the increase of the source separation is also maximum at the tube's center point. Since we focus here on comparing the tube geometry to the string profile rather than the laws of growth, we circumvent any ambiguity in measuring a model's fit parameters [Eq. (19)] by measuring the change in the width of the tube at each corresponding plane with respect to the central plane x_0,

$$\delta w^2 = w^2(x_i) - w^2(x_0). \tag{28}$$

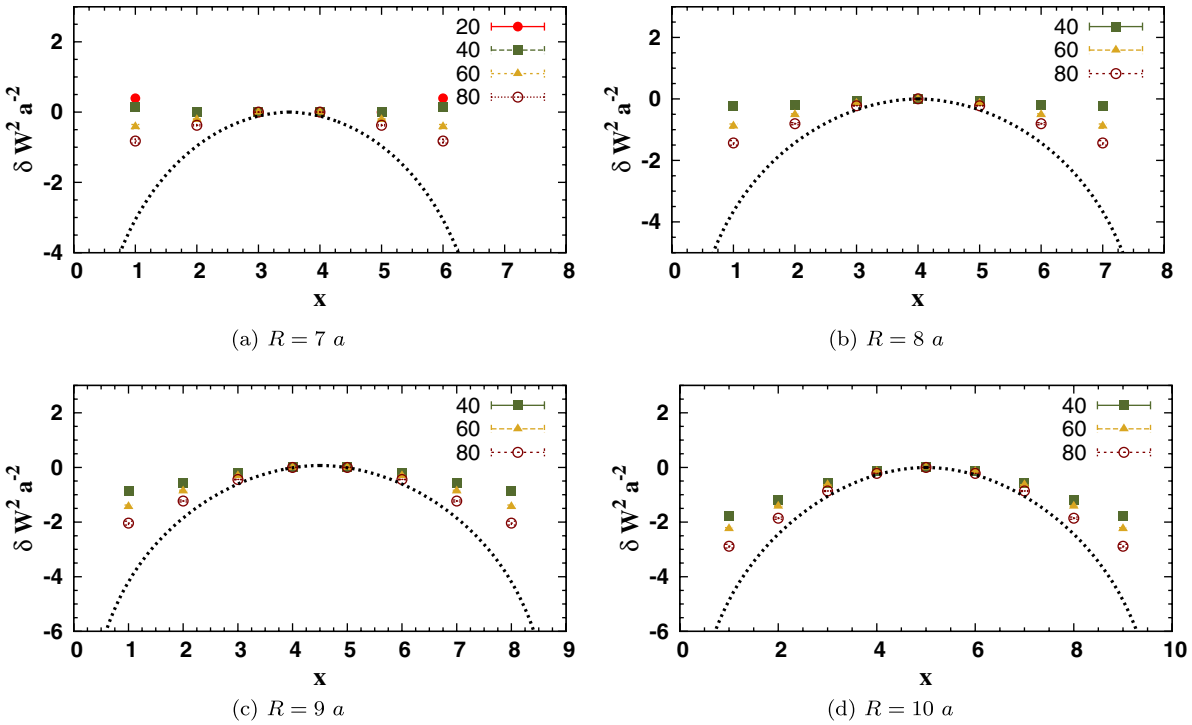

FIG. 10 (color online). The width difference $\delta w^2 = w^2(x_i) - w^2(x_0)$ for $q\bar{q}$ separations (a) 0.7 fm, (b) 0.8 fm, (c) 0.9 fm, and (d) 1 fm, $\beta = 6$, $T = 0.9T_C$ for each depicted smearing level. The line denotes the width difference δw^2 as predicted by the string model Eq. (19). The lowest smearing level provides the best estimate of the width difference.

This can provide a measure on how rounded or squeezed the flux tube would be compared to the width of the string fluctuations. Figure 10 shows the change in the tube width calculated for separation distance $R = 0.7$ fm to $R = 0.9$ fm, with uncertainties taken such that the standard errors in the Gaussian fits are correlated, i.e., $| e(x_i) - e(x_0) |$. In contrast with the predictions of the string model, the tube has an almost constant width at $R \leq 0.8$ fm. The measured changes in width at the plane $x = 1$ deviate from that of the model at $R = 0.9$ fm by a large value of 75%. The deviations decrease as the sources are pulled apart to 50% at $R = 1.0$ fm, 25% at $R = 1.2$ fm, and good agreement between both profiles is reached at $R = 1.3$ fm and $R = 1.4$ fm as can be seen in Fig. 11. The change of the width measured at the inner-transverse planes, however, agrees with the model at shorter distances, $R = 1.2$ fm for the plane $x = 2$ and $x = 3$. In general, the four plots in Fig. 11 show significant improvement with respect to the model predictions compared to the four plots at shorter distances in Fig. 10. The flux tube shows an almost constant cross-section for $R = 0.8$ fm in disagreement with the string picture. At distances 0.8 fm $< R < 1.1$ fm, the lattice gluonic-distribution profile is, geometrically speaking, more squeezed than the free-string picture would imply. As the sources are pulled farther apart, the disagreement decreases gradually and the profiles of the glue and the string both compare well for sources' separations $R \gtrsim 1.2$ fm.

To show the effects of smearing on the tube profile, the data corresponding to all smearing levels are included in Figs. 10 and 11. The lattice data indicate similar topology for the flux tube for the analysis on 20 and 40 sweeps of smearing at distance $R = 0.7$ fm. For smearing levels of 40 and 60 sweeps, the measurements are revealing the same topolgy for $R \gtrsim 0.9$ fm. All smearing levels are yielding the same flux-tube structure as can be seen in Fig. 11 for distance scales $R \gtrsim 1.1$ fm. This is consistent with our earlier assertion of a general distance scale, $\gamma = 2R_s$, which commences 2 times the radius of the Brownian motion Eq. (23), as a range which is free of smearing effects. For source separations where the tube geometry is clearly affected by smoothing, as can be seen in Fig. 10, the largest deviations from the model predictions do occur at the lowest level of smearing where the short distance physics is best preserved. The increase in agreement between the model prediction and lattice data at short distances $0.6 \leq R \leq 1.0$ fm for measurements taken on highly smoothed gauge configurations is, however, an interesting observation in its own right with physical implications that will be studied in detail elsewhere [31].

The thermal effects are manifest in the gluonic profile, giving rise to nonuniform widths. The string picture can parametrize these profiles only at large distances. At short distances on the other hand, the free-string picture does not model the gluonic interactions on the scale of short

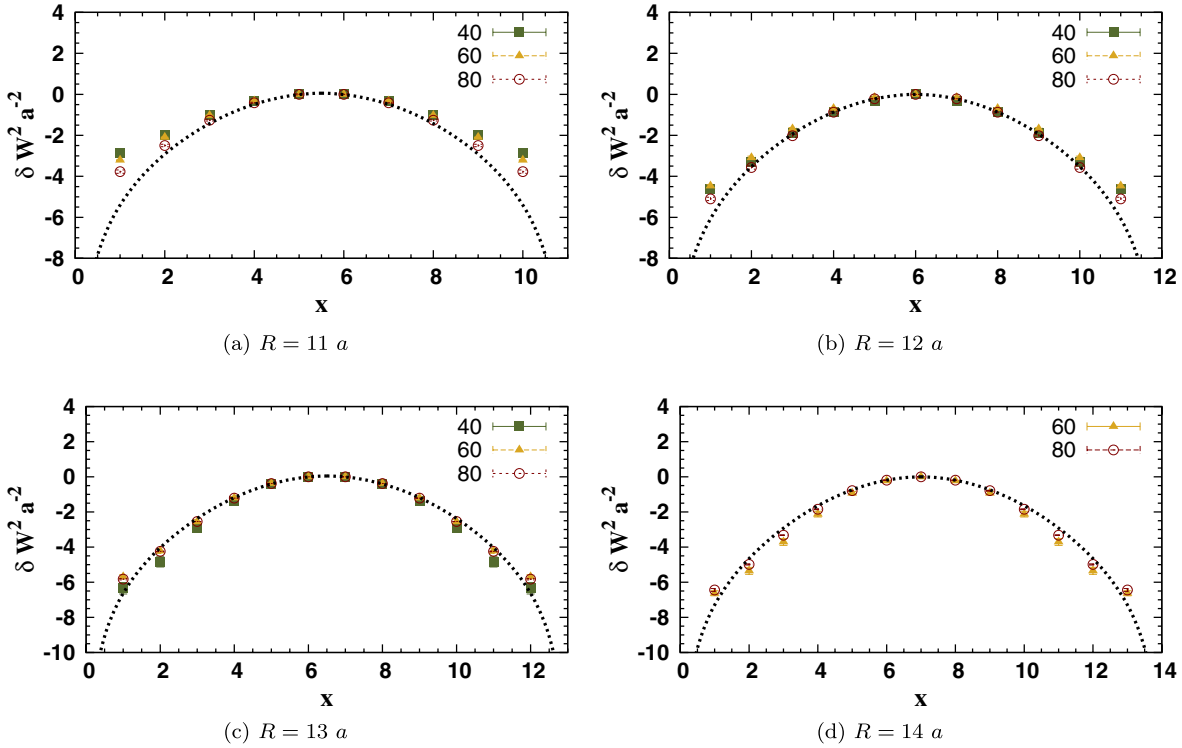

(a) $R = 11\ a$ (b) $R = 12\ a$

(c) $R = 13\ a$ (d) $R = 14\ a$

FIG. 11 (color online). Similar to Fig. 10, the change in width is plotted for $q\bar{q}$ separations (a) 1.1 fm, (b) 1.2 fm, (c) 1.3 fm, and (d) 1.4 fm.

TABLE VI. The resultant measurements of the scale R_0 for the first four consecutive transverse planes x_i in accord to the fits of the tube width to the string model formula Eq. (19). The values of the fit parameter, R_0, and the corresponding $\chi^2_{\rm dof}$ are presented for a variety of fit ranges.

	$x=1$		$x=2$		$x=3$		$x=4$	
Plane fit range	$R_0 a^{-1}$	$\chi^2_{\rm dof}$	$R_0 a^{-1}$	$\chi^2_{\rm dof}$	$R_0 a^{-1}$	$\chi^2_{\rm dof}$	$R_0 a^{-1}$	$\chi^2_{\rm dof}$
6–10	0.017(4)	7.3	0.030(6)	8.2	0.040(9)	8.7		
6–13	0.013(3)	9.5	0.023(5)	12.9	0.029(7)	15.6		
7–13	0.010(2)	4.9	0.019(3)	8.3	0.024(6)	12.1		
8–13	0.0093(8)	2.5	0.016(3)	6.1	0.019(4)	7.9	0.018(4)	8.9
9–13	0.0082(8)	1.1	0.013(1)	2.7	0.016(3)	4.2	0.016(3)	6.7
10–13	0.0074(4)	0.3	0.011(1)	1.0	0.013(1)	1.7	0.013(3)	4.9

distances which may become even more relevant in the thermal regime [31].

3. Tube growth in width

The measured values in Tables IV and V indicate a growth in the tube's mean-square width at all transverse planes x_i as the color sources are pulled apart. The growth in flux-tube width at each selected transverse plane can be compared to the corresponding growth in the string fluctuation Eq. (19); this comparison can be performed by fitting the formula of Eq. (19) to the tube measured widths. Table VI summarizes the resultant measurements of the fit parameter and the corresponding $\chi^2_{\rm dof}$ at four consecutive transverse planes $x=1$ to $x=4$. The fits show strong dependency on the fit range if the points at small sources' separations are included. The highest value of χ^2 is returned when fits include the whole range of sources' separations, i.e., $R=6a$ to $R=13a$. With the first four points excluded from the fit, the returned $\chi^2_{\rm dof}$ is smaller, indicating that only the data points at large source separation are parametrized by the string model formula. The value of the $\chi^2_{\rm dof}$ gradually decreases as we exclude points at short distance separations, and stability in the fit is reached for widths measured for the plane $x=1$ at sources'

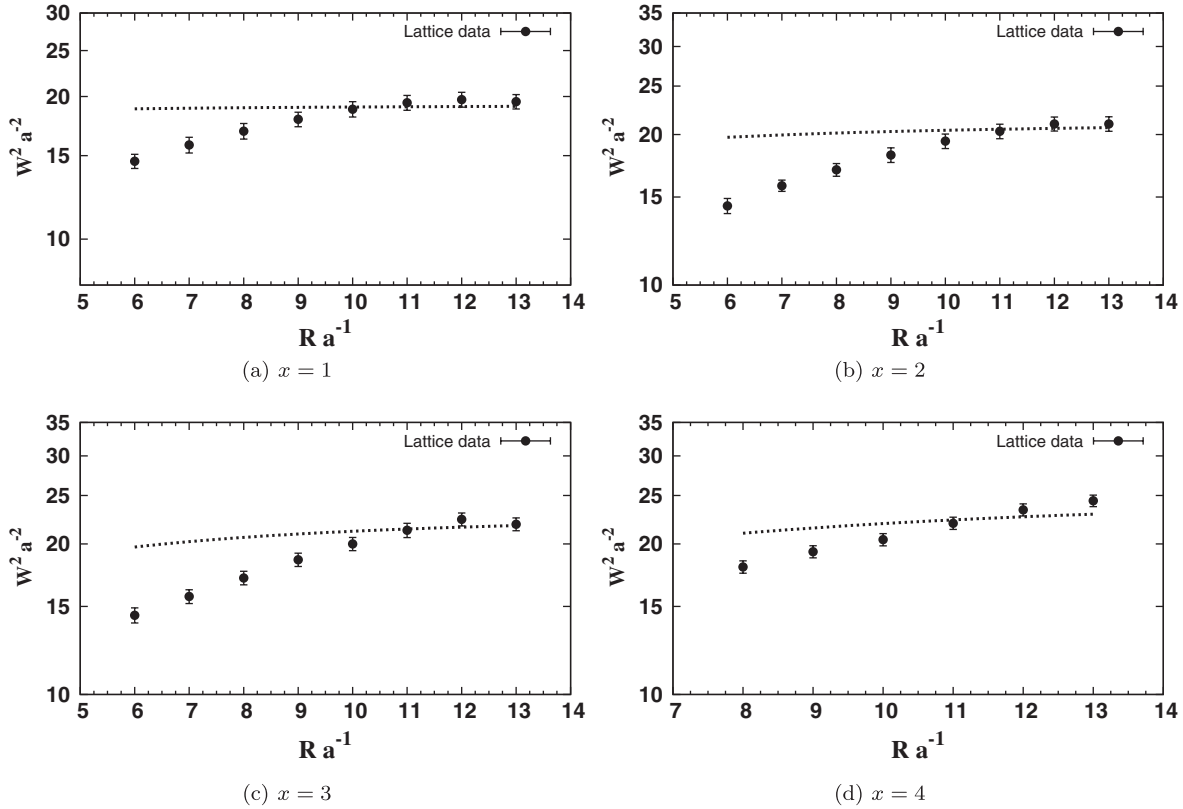

(a) $x=1$ (b) $x=2$ (c) $x=3$ (d) $x=4$

FIG. 12. The width $w^2(x_i)$ for $q\bar{q}$ separations $R=6a$ to $R=13a$ at four consecutive planes (a) $x=1$, (b) $x=2$, (c) $x=3$, and (d) $x=4$. $\beta=6$, $T=0.9T_C$. The line denotes the string model, Eq. (19), fit of R_0 to the data as described in the text.

separations $R > 0.7$ fm, and at $R > 0.8$ fm for the plane $x = 2$. The fits are returning good $\chi^2_{\rm dof}$ values for fits at the planes $x = 3, 4$ for sources' separations $R \geq 0.9$ fm. In the regions where the fits are returning good $\chi^2_{\rm dof}$, the values of the fit parameters are almost equal for the planes in the middle, $x = 2, 3, 4$. However, at the closest plane to the sources, $x = 1$, the value of the returned parameter, unsurprisingly, deviates from the corresponding one at other planes. This is another manifestation of the above observed deviations in the change in tube widths at this plane compared to the central plane as emphasized in the discussion surrounding Figs. 10 and 11.

Figure 12 shows data points and the corresponding best fits to the string model at each plane; the string model at finite temperature poorly describes the lattice data at short distances. The plots depict the fact that the flux tube observed in lattice gauge theory has a more suppressed profile than the fluctuations of the free string would imply at short distances. On the other hand, the growth of the flux-tube diameter is manifest in the lattice data.

V. CONCLUSION

The gluonic distribution inside the static meson has been revealed at finite temperature. The Monte Carlo simulations have been performed on the SU(3) gauge group for temperatures $T \simeq 0.8T_c$ and $T \simeq 0.9T_c$. Noise reduction has been achieved by a gauge-independent high statistics approach, in addition to the employment of adequate levels of gauge smoothing that preserve the relevant physics at large distances. This method is variant to noise reduction by Abelian gauge fixing. The flux tube, characterized as a correlation between the action density and the mesonic operator (Polyakov lines), has been displayed up to distances of 1.4 fm. The flux isolines and isosurfaces display a curved profile along the tube. The profile is showing a nonuniform action-density pattern unlike that observed using Wilson's loop as a mesonic operator at $T = 0$. The flux-tube width profile is compared to the corresponding mean-square width of the free bosonic string fluctuations at all planes between the color sources. For source separation distances $R > 0.8$ fm, measurements of the tube cross-section at each selected transverse plane show a nonconstant width for the tube, with maximum width at the symmetry point of the tube. At small $q\bar{q}$ source separations $0.8 \text{ fm} < R < 1.1$ fm, the tube is seen to yield a more compact (squeezed) form than the string model would predict. The deviations of the tube width profile from the corresponding string profile decrease gradually as the source separation increases. The profiles compare well at $R \simeq 1.2$ fm.

The gluonic profiles displayed in this investigation are geometric manifestations of thermal effects on the $q\bar{q}$ potential (the measured decrease in the string tension). Moreover, the squeezed gluonic profile in comparison to the rounded string fluctuations provides a geometrical interpretation for the deviations of the predicted string tension based on the free-string picture from the corresponding lattice results [1].

This study is motivating further investigations of the energy-density and chromoelectromagnetic distributions with methodological improvements that minimize the number of smearing sweeps and increase the number of measurements. It would also be interesting to confront these profiles with the bosonic string profiles in the context of string self-interactions. The string's geometrical effects (curved profiles) ought to be addressed in other gauge groups. Work is progressing in these directions, in addition to the detailed investigation of the thermal hadronic gluonic distributions by straightforward generalizations of the calculations presented here to baryons [43,44].

ACKNOWLEDGMENTS

Thanks to Tom Cohen for providing useful comments. We also thank Dimitri Diankov for encouragement to conduct the investigation. This work has been done using the supercomputing resources from the NCI National Facility and eResearch SA. The three-dimensional and two-dimensional realizations have been rendered in the eResearch SA Visualization Lab.

APPENDIX A: SMEARING RADIUS

In the standard APE smearing, a smearing sweep consists of a replacement of the link variable $U_\mu(x)$ ($\mu = 1, 2, 3, 4$) by the $\mathrm{SU}(3)_c$ projected link $\bar{U}_\mu(x)$ that maximizes the trace

$$\mathrm{Re\ Tr}\{\bar{U}_\mu(x) U^\dagger_{s,\mu}(x)\}, \tag{A1}$$

where

$$U_{s,\mu}(x) = (1-\alpha)U_\mu(x) + \frac{\alpha}{6}\sum_{\mu\neq\nu}\{U_\nu(x)U_\mu(x+\hat{\nu}) \times U^\dagger_\nu(x+\hat{\mu}) + U^\dagger_\nu(x-\hat{\nu})U_\mu(x-\hat{\nu}) \times U_\mu(x+\hat{\nu}-\hat{\mu})\}, \tag{A2}$$

where α is the smearing parameter. Consider, by analogy, a scalar field $\phi(\mathbf{r}; n+1)$ similar to the $(n+1)$th smeared gauge link in the μ direction. It is related to the scalar field $\varphi(\mathbf{r}; n)$ at the n smearing time by correspondence to Eq. (A2) via

$$\phi(\mathbf{r}; n+1) = (1-\alpha)\phi(\mathbf{r}; n) + \frac{\alpha}{6}\sum_{\nu\neq\mu}(\phi(\mathbf{r}+a\hat{\nu}; n) + \phi(\mathbf{r}-a\hat{\nu}; n)). \tag{A3}$$

Introducing a smearing time $\tau = na_\tau$ with a spacing a_τ, the finite difference smearing operator can be approximated by $\Delta_n \simeq a_\tau \partial_\tau$. Applying this operator into Eq. (A3) yields

$$\partial_\tau \phi(\mathbf{r};\tau) \simeq \frac{a}{a_\tau}\frac{\alpha}{6}\sum_{\nu\neq\mu}(\partial_\nu\phi(\mathbf{r};\tau) + \partial_\nu\phi(\mathbf{r}-a\nu;\tau)). \tag{A4}$$

It follows that

$$\partial_\tau \phi(\mathbf{r};\tau) = D\nabla^2\phi(\mathbf{r};\tau),$$

with the diffuseness,

$$D \equiv \frac{\alpha}{6}\frac{a^2}{a_\tau}. \tag{A5}$$

The unsmeared field corresponds to source,

$$\phi(\mathbf{r}; n=0) = \delta(\mathbf{r}). \tag{A6}$$

The solution of the above initial value problem, Eqs. (A6) and (A5), is a Green function of the heat equation Eq. (A5). This gives the evolution of the scalar field in the smearing time,

$$G(\mathbf{r};\tau) = \frac{1}{(4\pi D\tau)^{3/2}}\exp\left[-\frac{\mathbf{r}.\mathbf{r}}{4D\tau}\right]. \tag{A7}$$

The diffuse field is Gaussian distributed through a sphere with a characteristic radius,

$$R_s \equiv \left(\frac{\int d^3\mathbf{r}G(\mathbf{r};\tau)\mathbf{r}^2}{\int d^3\mathbf{r}G(\mathbf{r};\tau)}\right)^{1/2} = a\sqrt{\alpha n}. \tag{A8}$$

APPENDIX B: CALIBRATION OF SMOOTHING ALGORITHMS

Calibrating different smearing algorithms can proceed via comparing the respective number of smearing sweeps in each smearing scheme with respect to a certain threshold [35]. The reconstructed action density [16] normalized to a single instanton action S/S_0 is the threshold adopted here. Figure 13 shows the relative number of smearing sweeps for different values of the stout-link smearing parameter ρ compared to that at $\rho = 0.06$ in the improved stout-link smearing algorithm [18], with $\epsilon = -0.25$. Assuming that the number of smearing sweeps scales with the smearing parameter as

$$\frac{n_s(\rho_2)}{n_s(\rho_1)} = \left(\frac{\rho_1}{\rho_2}\right)^\delta, \tag{B1}$$

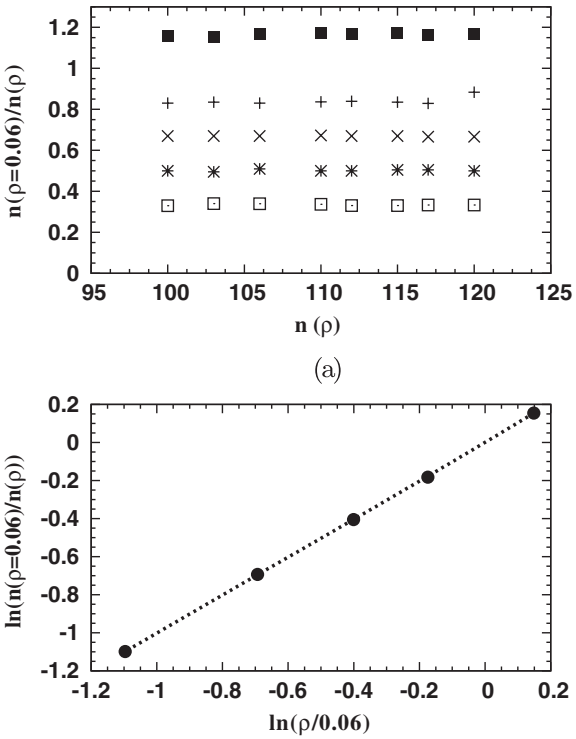

FIG. 13. (a) $n(0.06)/n(\rho)$ versus $n(\rho)$ for $\rho = 0.07, 0.05, 0.04, 0.03$, and 0.02 from top to bottom. (b) Plot of logarithm of the average value of $n(\rho = 0.06)/n(\rho)$ versus $\ln(\rho/0.06)$; the line corresponds to fit to a straight line passing through the origin.

the fit of the logarithm of both sides in Eq. (B1) to a straight line yields a slope $\delta = 1$ as is depicted in Fig. 13. The number of sweeps in the improved stout-link smearing, therefore, scales inversely with the smearing parameters. The standard APE smearing shows also the same scaling behavior [35] and both algorithms can be calibrated through

$$\frac{\alpha n_{\mathrm{ape}}(\alpha)}{\rho n_s(\rho)} = c. \tag{B2}$$

Calibration with respect to APE smearing at $\alpha = 0.7$ yields the proportionality constant $c = 6.15(3)$. Using Eq. (A8) gives $R_s = a\sqrt{\rho c n_s}$.

[1] O. Kaczmarek, F. Karsch, E. Laermann, and M. Lutgemeier, Phys. Rev. D **62**, 034021 (2000).
[2] M. Luscher, K. Symanzik, and P. Weisz, Nucl. Phys. **B173**, 365 (1980).
[3] M. Luscher and P. Weisz, J. High Energy Phys. 07 (2002) 049.
[4] G. S. Bali, C. Schlichter, and K. Schilling, Phys. Rev. D **51**, 5165 (1995).

[5] K. J. Juge, J. Kuti, and C. Morningstar, Phys. Rev. Lett. **90**, 161601 (2003).
[6] M. Caselle, F. Gliozzi, U. Magnea, and S. Vinti, Nucl. Phys. **B460**, 397 (1996).
[7] M. Caselle, M. Pepe, and A. Rago, J. High Energy Phys. 10 (2004) 005.
[8] P. de Forcrand, G. Schierholz, H. Schneider, and M. Teper, Phys. Lett. **160B**, 137 (1985).
[9] M. Gao, Phys. Rev. D **40**, 2708 (1989).
[10] M. Caselle, M. Panero, P. Provero, and M. Hasenbusch, Nucl. Phys. B, Proc. Suppl. **119**, 499 (2003).
[11] M. Luscher, G. Munster, and P. Weisz, Nucl. Phys. **B180**, 1 (1981).
[12] P. Pennanen, A. M. Green, and C. Michael, Phys. Rev. D **56**, 3903 (1997).
[13] F. Gliozzi, M. Pepe, and U. J. Wiese, Phys. Rev. Lett. **104**, 232001 (2010).
[14] A. Allais and M. Caselle, J. High Energy Phys. 01 (2009) 073.
[15] T. Heinzl *et al.*, Phys. Rev. D **78**, 034504 (2008).
[16] S. O. Bilson-Thompson, D. B. Leinweber, and A. G. Williams, Ann. Phys. (N.Y.) **304**, 1 (2003).
[17] C. Morningstar and M. Peardon, Phys. Rev. D **69**, 054501 (2004).
[18] P. J. Moran and D. B. Leinweber, Phys. Rev. D **77**, 094501 (2008).
[19] F. Bissey *et al.*, Phys. Rev. D **76**, 114512 (2007).
[20] V. G. Bornyakov, H. Ichie, Y. Mori, D. Pleiter, M. I. Polikarpov, G. Schierholz, T. Streuer, H. Stüben, and T. Suzuki, Phys. Rev. D **70**, 054506 (2004).
[21] K. Fabricius and O. Haan, Phys. Lett. **143B**, 459 (1984).
[22] A. D. Kennedy and B. J. Pendleton, Phys. Lett. **156B**, 393 (1985).
[23] N. Cabibbo and E. Marinari, Phys. Lett. **119B**, 387 (1982).
[24] W. Detmold and M. J. Savage, Phys. Rev. Lett. **102**, 032004 (2009).
[25] S. Thurner, M. Feurstein, H. Markum, and W. Sakuler, Phys. Rev. D **54**, 3457 (1996).
[26] P. Olesen, Phys. Lett. **160B**, 144 (1985).
[27] F. Gliozzi, in *Quark Confinement 1994* (World Scientific, Singapore, 1995).
[28] J. S. Schwinger, Phys. Rev. **82**, 914 (1951).
[29] It is worth noting that by the use of a link integration method [30], one would not expect a factor of error reduction that can be more than $x \simeq 1.1$ in the middle region. For larger distances, however, the link integration method would be beneficial only if supplemented by a large number of measurements.
[30] P. de Forcrand and C. Roiesnel, Phys. Lett. **151B**, 77 (1985).
[31] A. Bakry, D. Leinweber, and A. Williams, "Thermally Delocalized Flux Tubes in Mesons and Baryons," in STRONGnet 2010 Conference Hadron Physics in Lattice QCD, Paphos, 2010.
[32] R. Sommer, Nucl. Phys. **B411**, 839 (1994).
[33] M. Albanese *et al.* (APE), Phys. Lett. B **192**, 163 (1987).
[34] T. T. Takahashi, H. Suganuma, Y. Nemoto, and H. Matsufuru, Phys. Rev. D **65**, 114509 (2002).
[35] F. D. R. Bonnet, D. B. Leinweber, A. G. Williams, and J. M. Zanotti, Phys. Rev. D **65**, 114510 (2002).
[36] Y. Peng and R. W. Haymaker, Phys. Rev. D **47**, 5104 (1993).
[37] T. Doi, N. Ishii, M. Oka, and H. Suganuma, Nucl. Phys. B, Proc. Suppl. **140**, 559 (2005); in Lattice 2004, 22nd International Symposium on Lattice Field Theory, Batavia, Illinois, 21–26 June 2004.
[38] The ground-state source-wave functions in the Wilson-loop operator are trial-wave functions, and the state adopted is the one which maximizes the overlap with the ground state, usually by smearing the string of the glue connecting the quarks [4,15]. Moreover, the calculations of gluonic distribution are plagued by systematic errors due to biasing by the shape of the source, and the corresponding limitations imposed by the statistical fluctuations upon the Euclidean-time evolution in the loop operator [19,39].
[39] F. Okiharu and R. M. Woloshyn, Nucl. Phys. B, Proc. Suppl. **129–130**, 745 (2004).
[40] G. Parisi, Phys. Rev. D **11**, 970 (1975).
[41] G. 't Hooft, in *High Energy Physics*, edited by A. Zichichi (EPS International Conference, Palermo, 1975).
[42] S. Mandelstam, Phys. Rep. **23**, 245 (1976).
[43] A. S. Bakry, in AIP Congress, Adelaide, 30 Nov.–5 Dec. 2008.
[44] A. S. Bakry, "Gluon Flux Distribution in Baryons at Finite Temperature," in T(R)OPICAL QCD, Cairns, 2008.